Nuclear Pore Scaffold Structure Analyzed by Super-Resolution Microscopy and Particle Averaging

Anna Szymborska *et al.*
Science **341**, 655 (2013);
DOI: 10.1126/science.1240672

Nuclear Pore Scaffold Structure Analyzed by Super-Resolution Microscopy and Particle Averaging

Anna Szymborska,[1] Alex de Marco,[2] Nathalie Daigle,[1] Volker C. Cordes,[3] John A. G. Briggs,[2] Jan Ellenberg[1]*

Much of life's essential molecular machinery consists of large protein assemblies that currently pose challenges for structure determination. A prominent example is the nuclear pore complex (NPC), for which the organization of its individual components remains unknown. By combining stochastic super-resolution microscopy, to directly resolve the ringlike structure of the NPC, with single particle averaging, to use information from thousands of pores, we determined the average positions of fluorescent molecular labels in the NPC with a precision well below 1 nanometer. Applying this approach systematically to the largest building block of the NPC, the Nup107-160 subcomplex, we assessed the structure of the NPC scaffold. Thus, light microscopy can be used to study the molecular organization of large protein complexes in situ in whole cells.

Methods used to determine the structures of large complexes in situ, for example, electron tomography, currently lack the resolution for direct molecular assignments. Consequently, structure determination of very large protein assemblies, such as the nuclear pore complex (NPC), is extremely challenging. The NPC channel mediates nucleocytoplasmic transport, consists of several hundred proteins termed nucleoporins (Nups), and has an estimated mass of 110 MD (*1*). Despite progress in the crystallization of individual Nups (*2*, *3*) and electron tomographic reconstruction of the whole NPC (*4*, *5*), it remains unclear how the individual proteins are organized within the complex. Super-resolution (SR) fluorescence microscopy should be able to fill this gap, because it combines specific molecular labeling with a very high resolution (*6*). However, SR imaging of biological structures in situ is currently limited to a resolution of ~15 nm (*6–8*). We reasoned that it should be possible to improve the precision of SR microscopy by combining many SR images of individual complexes using single-particle averaging and applied this approach to address the structural organization of the NPC.

We first established a robust methodological pipeline by using Nup133, a stable component of the NPC scaffold. Stochastic localization microscopy (*7–12*) of antibody-labeled Nup133 achieved about one order of magnitude better resolution than state-of-the-art confocal microscopy (Fig. 1, A and B) and revealed that Nup133 molecules are organized in a ring, consistent with previous observations of the transmembrane Nup gp210

(*13*). The large field of view of the SR light microscope allowed us to record the entire lower surface of a mammalian nucleus, typically containing several hundred pores with their transport axes oriented along the optical axis. Next, we developed a single-particle averaging routine that allowed us to combine information from thousands of pores (Fig. 1, C to F) (*14*). After passing stringent quality control (figs. S1 and S2), the particles were aligned and summed to generate an average image of the respective fluorescent

label in the NPC (Fig. 1, C and D). From the mean radial intensity profile of the image, we could determine the average position of the fluorescent label with respect to the center of the pore with a standard deviation of 0.1 nm (Fig. 1, E and F, and fig. S3). Applying the averaging pipeline to simulated particles showed that our method underestimated the real position of the label by 0.3 nm owing to incomplete decoration of the pore ring (fig. S4). Thus, we could determine the average radial position of the fluorescent label with a precision of 0.1 nm and an accuracy of 0.3 nm.

Next, we applied our method to systematically probe the molecular organization of the human NPC scaffold, which is primarily composed of multiple copies of the Nup107-160 subcomplex, a stable assembly of nine Nups. On the basis of structural homology, the organization of the human (hs) subcomplex is generally assumed to be similar to the yeast (y) Nup84 subcomplex, which resembles a 40-nm-long letter Y (*15*, *16*). The positions and orientations of the yeast proteins within the Y shape have been assigned on the basis of biochemical and crystallographic data (*17*) (Fig. 2A). The stalk of the complex is formed by yNup133 (hsNup133) at the foot, followed by yNup84 (hsNup107) and yNup145C-ySec13 (hsNup96-hsSec13) at the central branch point. The two arms contain yNup120 (hsNup160) and yNup85-ySeh1 (hsNup85-hsSeh1), respectively. The human complex additionally contains Nup37, which localizes to the Nup160 arm, and Nup43, whose position is thus far undetermined.
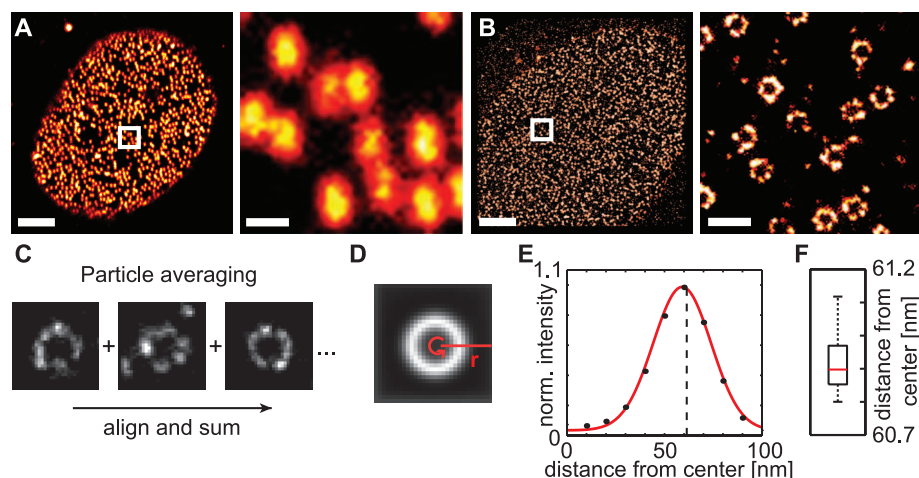

Fig. 1. SR microscopy combined with single-particle averaging. (A) Confocal and **(B)** SR microscopy of U2OS cells stained with Nup133 antibody raised against the full-length protein (FL), showing the lower surface of the nucleus (left) and a magnified 2-μm^2 area (right). Scale bars (SB) indicate 3 μm and 300 nm, respectively. **(C)** Examples of Nup133-FL–labeled pores that passed quality control. **(D)** Average image of the NPC, generated by summing of 8698 quality-controlled and translationally aligned particles. The mean radial intensity profile of the image was calculated by averaging the line profile r in all directions. **(E)** Normalized mean radial intensity profile (black points) fitted with circularly convolved Gaussian (red line). Summing of several two-dimensional (2D) Gaussian peaks in a circle results in an apparent shift of the peak toward the center of the pore. The true mean radial position of the fluorescence label (dashed line) can be determined from the fit. **(F)** Precision of determining the radial position was estimated by cross-validation, performed by averaging 17 sets of 500 pores each (red line marks the median). The standard deviation of the distribution is 0.1 nm. The whiskers on the box plot encompass 99.3% of the distribution.

[1]Cell Biology and Biophysics Unit, European Molecular Biology Laboratory, Meyerhofstrasse 1, 69117 Heidelberg, Germany. [2]Structural and Computational Biology Unit, European Molecular Biology Laboratory, Meyerhofstrasse 1, 69117 Heidelberg, Germany. [3]Max Planck Institute for Biophysical Chemistry, Am Fassberg 11, 37077 Göttingen, Germany.
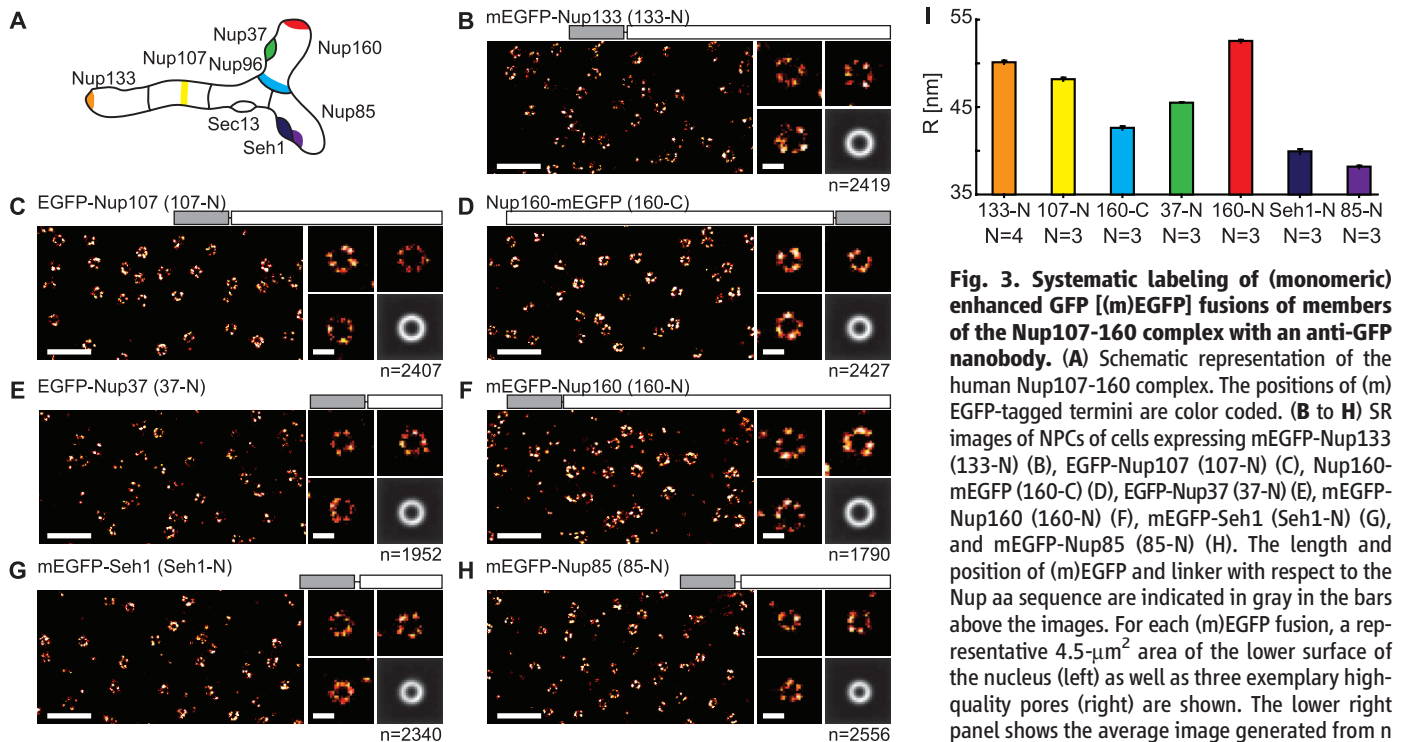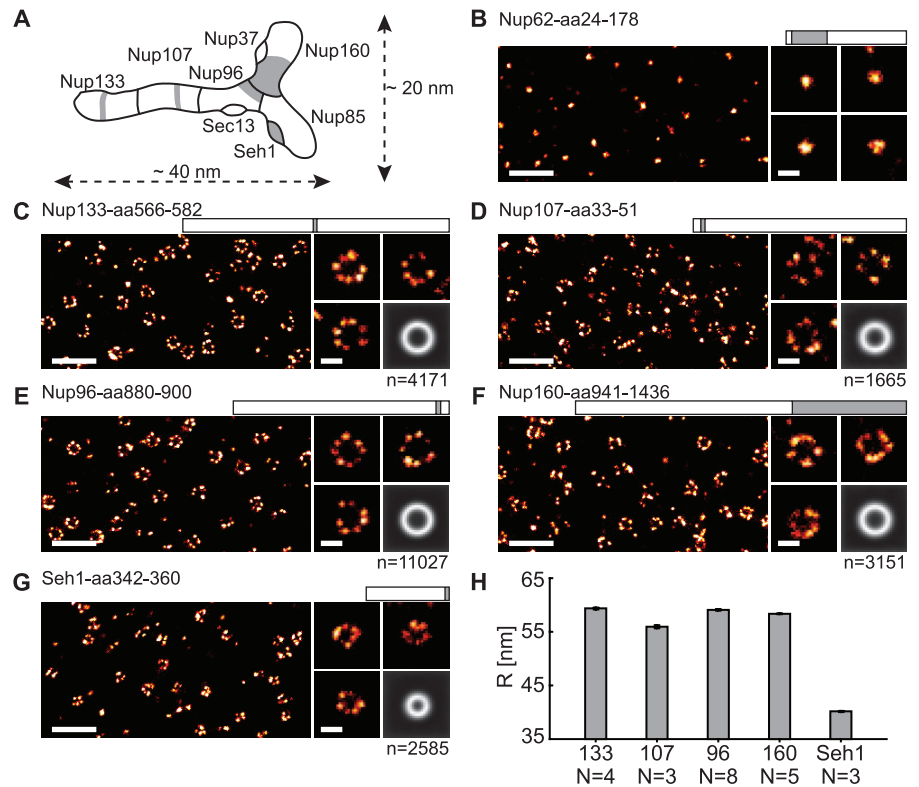
*Corresponding author. E-mail: jan.ellenberg@embl.de

At least three contradictory models for the orientation of the Nup107-160 subcomplex have been proposed, each making different predictions for the radial position of its components at the scale of nanometers (*18–20*) (fig. S5). To address this, we first attempted to localize endogenous Nup107-160 complex members by using antibodies. We could specifically label the stalk (Nup133 and Nup107), the central branch point (Nup96), and each arm of the Y (Seh1 and Nup160). As expected, all five components of the subcomplex appeared as ring structures in SR images

Fig. 2. Systematic immunolabeling of the Nup107-160 complex. (**A**) Schematic representation of the current model of the human Nup107-160 complex based on homology to the yeast Nup84 subcomplex (Nup43 is omitted, because its position is not known). The dimensions of the yeast complex are indicated. The approximate positions of the antigens of the antibodies used in this study are indicated in gray. (**B** to **G**) SR images of NPCs stained with antibodies against Nup62 (B), Nup133 (C), Nup107 (D), Nup96 (E), Nup160 (F), and Seh1 (G). The bars above the images show the position of the antigen (gray) with respect to the rest of the amino acid (aa) sequence. For each antibody, a representative 4.5-μm² area of the lower surface of the nucleus (left) is shown, as well as four (B) or three [(C) to (G)] exemplary high-quality pores (right). The lower right panel in (C) to (G) shows the average image, generated from *n* number of aligned pores. SB, 0.5 μm and 0.1 μm. (**H**) Average radial positions *R* of the antibody-stained Nups measured in *N* independent experiments. The error bars represent SEM of the experiments. From left to right: Nup133-aa566-582 *R* = 59.4 ± 0.2 nm (SEM), Nup107-aa33-51 *R* = 55.9 ± 0.3 nm, Nup96-aa880-900 *R* = 59.0 ± 0.1 nm, Nup160-aa941-1436 *R* = 58.3 ± 0.2 nm, Seh1-aa342-360 *R* = 40.4 ± 0.3 nm. Positions of Nup107 and Seh1 are significantly different from all other positions with a *t* test *P* value *P* < 0.01.

Fig. 3. Systematic labeling of (monomeric) enhanced GFP [(m)EGFP] fusions of members of the Nup107-160 complex with an anti-GFP nanobody. (**A**) Schematic representation of the human Nup107-160 complex. The positions of (m)EGFP-tagged termini are color coded. (**B** to **H**) SR images of NPCs of cells expressing mEGFP-Nup133 (133-N) (B), EGFP-Nup107 (107-N) (C), Nup160-mEGFP (160-C) (D), EGFP-Nup37 (37-N) (E), mEGFP-Nup160 (160-N) (F), mEGFP-Seh1 (Seh1-N) (G), and mEGFP-Nup85 (85-N) (H). The length and position of (m)EGFP and linker with respect to the Nup aa sequence are indicated in gray in the bars above the images. For each (m)EGFP fusion, a representative 4.5-μm² area of the lower surface of the nucleus (left) as well as three exemplary high-quality pores (right) are shown. The lower right panel shows the average image generated from n number of aligned pores. SB, 0.5 μm and 0.1 μm.

(**I**) Average radial positions *R* of the GFP-tagged Nups measured in *N* independent experiments. From left to right: 133-N *R* = 50.1 ± 0.2 nm, 107-N *R* = 48.2 ± 0.2 nm, 160-C *R* = 42.6 ± 0.2 nm, 37-N *R* = 45.5 ± 0.0 nm, 160-N *R* = 52.5 ± 0.2 nm, Seh1-N *R* = 39.9 ± 0.3 nm, 85-N *R* = 38.2 ± 0.2 nm. All positions are significantly different from all others with a *t* test *P* < 0.01.

(Fig. 2, C to G), in contrast to Nup62, a component of the central transport channel, which appeared as a spot (Fig. 2B). Differences in the diameters of some of the Nup107-160 components were evident in single SR images without averaging (Fig. 2, C to G). After averaging, we found that Nup133 is the outermost epitope, followed by Nup96, then Nup160, Nup107, and lastly Seh1 (Fig. 2H and fig. S6). The antibody-based localizations suggested that the stalk and the Nup160 arm of the Y are largely peripheral, whereas the Nup85-Seh1 arm reaches far to the center of the pore.

Despite the subnanometer precision and accuracy in determining the mean position of the fluorescent label, the substantial size of the primary and secondary antibody complexes could potentially offset the fluorescent dye from the targeted epitope. In addition, we could not obtain antibodies of sufficient quality for SR imaging against several Nup107-160 complex members. To systematically determine the positions of the components of the subcomplex with higher accuracy, we labeled a collection of seven Nup–green fluorescent protein (GFP) fusions with dye-coupled small anti-GFP nanobodies (21) (Fig. 3). To ensure high incorporation of the GFP-tagged protein into the pore and control for functionality, we depleted the endogenous Nups by RNA interference (14). Overall, the nanobody measurements resulted in a radial order of Nup107-160 complex members very similar to those obtained by using immunolabeling of endogenous Nups. The differences in absolute distances between the two labeling strategies that we observed for Nup133, Nup107, and Nup160 are consistent with the size difference between the nanobody and the bulky primary and secondary antibody pair, which becomes nonnegligible at this resolution.

The small error and well-defined average profile we measured for each protein suggested that they have very similar radial distances on the cytoplasmic and nucleoplasmic face of the pore, consistent with their symmetric localization along the transport axis (22), and that all copies of the subcomplex lie in a very similar orientation within the NPC (Fig. 3I). According to our subnanometer positional constraints for seven nanobody-labeled Nups, the Nup107-160 complex is arranged with its stalk tilting from the periphery slightly toward the center and splits at the branching point from where the Nup85-Seh1 arm reaches toward the center of the pore, whereas the Nup160-Nup37 arm stretches back toward the periphery (Fig. 4A and figs. S5D and S7). Our data are consistent with aspects of a previous computational model (20, 23) and with fluorescence anisotropy measurements (24), both of which proposed that the long axis of the Y-shaped complex is perpendicular to the direction of transport. Furthermore, our positional data does not support the "fence-like coat" (19, 25) (fig. S5B) or the "lattice" models (18, 26) (fig. S5C).

Comparison with the high-resolution human NPC cryogenic electron microscopy (cryo-EM) structure (5) placed most of our molecular positions in the electron density of the cytoplasmic and nucleoplasmic rings and excluded their localization in the spoke ring (Fig. 4B). The Nup85-Seh1 arm localizes at about the same radial distance as the eight pairs of central protrusions discernible in the cytoplasmic ring, while the rest of the Y shape overlaps with the ring backbone (Fig. 4C). Thus, a head-to-tail arrangement of Nup107-160 complex in cytoplasmic and nucleoplasmic rings, along the circumference of the pore, is the most likely model to explain our data. The model allows for the two proposed stoichiometries of 8 or 16 copies of the Nup107-160

complex per cytoplasmic or nucleoplasmic ring (22, 27, 28) (fig. S5D).

Although the alignment method we used to study the organization of the NPC relied on the intrinsic rotational symmetry of the complex, we demonstrated that it can be extended to asymmetric structures by aligning single particles on a molecular reference labeled in a second color without a loss of precision (figs. S8 and S9).

We combined stochastic SR microscopy with single-particle averaging to investigate the structure of a large protein complex, the NPC, in situ in whole cells. Our data provide direct evidence for the orientation of the Nup107-160 subcomplex within the pore and discriminate between contradictory models of the structural organization of the NPC scaffold. More generally, our results demonstrate that the average positions of fluorescence labels in protein complexes suitable for particle averaging can be determined by light microscopy with a precision well below 1 nm. This approach is potentially valuable to address structural biology questions pertaining to large protein complexes and organelles, including centrioles and the centrosome, endosomes, coated vesicles, and the kinetochore, because it bridges the gap between atomic resolution methods and label-free in situ techniques.

References and Notes

1. R. Reichelt et al., J. Cell Biol. 110, 883–894 (1990).
2. A. Hoelz, E. W. Debler, G. Blobel, Annu. Rev. Biochem. 80, 613–643 (2011).
3. S. G. Brohawn, J. R. Partridge, J. R. R. Whittle, T. U. Schwartz, Structure 17, 1156–1168 (2009).
4. M. Beck, V. Lucić, F. Förster, W. Baumeister, O. Medalia, Nature 449, 611–615 (2007).
5. T. Maimon, N. Elad, I. Dahan, O. Medalia, Structure 20, 998–1006 (2012).
6. L. Schermelleh, R. Heintzmann, H. Leonhardt, J. Cell Biol. 190, 165–175 (2010).
7. M. J. Rust, M. Bates, X. Zhuang, Nat. Methods 3, 793–796 (2006).
8. J. Fölling et al., Nat. Methods 5, 943–945 (2008).
9. E. Betzig et al., Science 313, 1642–1645 (2006).
10. S. T. Hess, T. P. K. Girirajan, M. D. Mason, Biophys. J. 91, 4258–4272 (2006).
11. H. Bock et al., Appl. Phys. B 88, 161–165 (2007).
12. M. Heilemann et al., Angew. Chem. Int. Ed. 47, 6172–6176 (2008).
13. A. Löschberger et al., J. Cell Sci. 125, 570–575 (2012).
14. For details, see supplementary materials available on Science Online.
15. M. Lutzmann, R. Kunze, A. Buerer, U. Aebi, E. Hurt, EMBO J. 21, 387–397 (2002).
16. M. Kampmann, G. Blobel, Nat. Struct. Mol. Biol. 16, 782–788 (2009).
17. S. Bilokapic, T. U. Schwartz, Curr. Opin. Cell Biol. 24, 86–91 (2012).
18. S. G. Brohawn, N. C. Leksa, E. D. Spear, K. R. Rajashankar, T. U. Schwartz, Science 322, 1369–1373 (2008).
19. K.-C. Hsia, P. Stavropoulos, G. Blobel, A. Hoelz, Cell 131, 1313–1326 (2007).
20. F. Alber et al., Nature 450, 695–701 (2007).
21. J. Ries, C. Kaplan, E. Platonova, H. Eghlidi, H. Ewers, Nat. Methods 9, 582–584 (2012).
22. M. P. Rout et al., J. Cell Biol. 148, 635–652 (2000).
23. J. Fernandez-Martinez et al., J. Cell Biol. 196, 419–434 (2012).
24. M. Kampmann, C. E. Atkinson, A. L. Mattheyses, S. M. Simon, Nat. Struct. Mol. Biol. 18, 643–649 (2011).
25. E. W. Debler et al., Mol. Cell 32, 815–826 (2008).
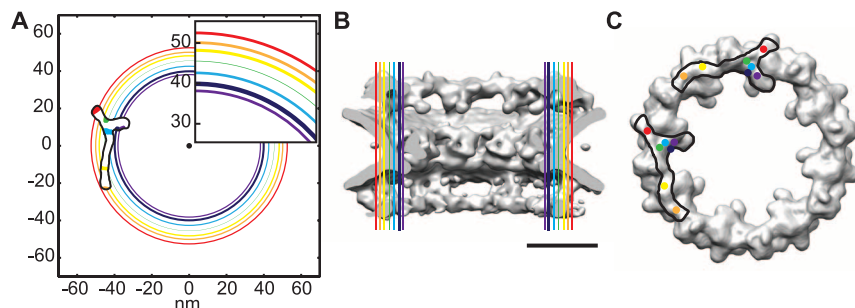26. S. Bilokapic, T. U. Schwartz, Proc. Natl. Acad. Sci. U.S.A. 109, 15241–15246 (2012).

Fig. 4. SR imaging–based model for the orientation of the Y-shaped complex in the NPC scaffold. (A) Average positions of (m)EGFP fusions of Nups 133-N (orange), 107-N (yellow), 160-C (light blue), 37-N (green), 160-N (red), Seh1-N (dark blue), and 85-N (purple) in the plane of the nuclear envelope, based on the spatial constraints from SR measurements of nanobody stained pores magnified in the inset. The line thickness represents the 95% confidence interval for the mean position of each tagged Nup. The schematic model of the Nup107-160 complex from Fig. 3A is brought into line with the measured positions. A cartoon illustrating the two equally possible opposite-handed models is shown in fig. S5D. **(B)** The mean positions of Nups overlaid to scale on the EM structure of the human NPC, viewed along the transport axis; SB, 40 nm. **(C)** Two possible arrangements of the Nup107-160 complexes traced in the electron density of the cytoplasmic ring of the nuclear pore consistent with our measurements; the dots are drawn in the measured radial position and adjusted manually along the circumference of the pore to mark the stalk and both arms of the Y shape.

27. J. M. Cronshaw, A. N. Krutchinsky, W. Zhang, B. T. Chait, M. J. Matunis, *J. Cell Biol.* **158**, 915–927 (2002).
28. A. Ori *et al.*, *Mol. Syst. Biol.* **9**, 648 (2013).

Polyploids Exhibit Higher Potassium Uptake and Salinity Tolerance in *Arabidopsis*

Dai-Yin Chao,[1] Brian Dilkes,[2] Hongbing Luo,[2] Alex Douglas,[1] Elena Yakubova,[2] Brett Lahner,[2] David E. Salt[1]*

Genome duplication (or polyploidization) has occurred throughout plant evolutionary history and is thought to have driven the adaptive radiation of plants. We found that the cytotype of the root, and not the genotype, determined the majority of heritable natural variation in leaf potassium (K) concentration in *Arabidopsis thaliana*. Autopolyploidy also provided resistance to salinity and may represent an adaptive outcome of the enhanced K accumulation of plants with higher ploidy.

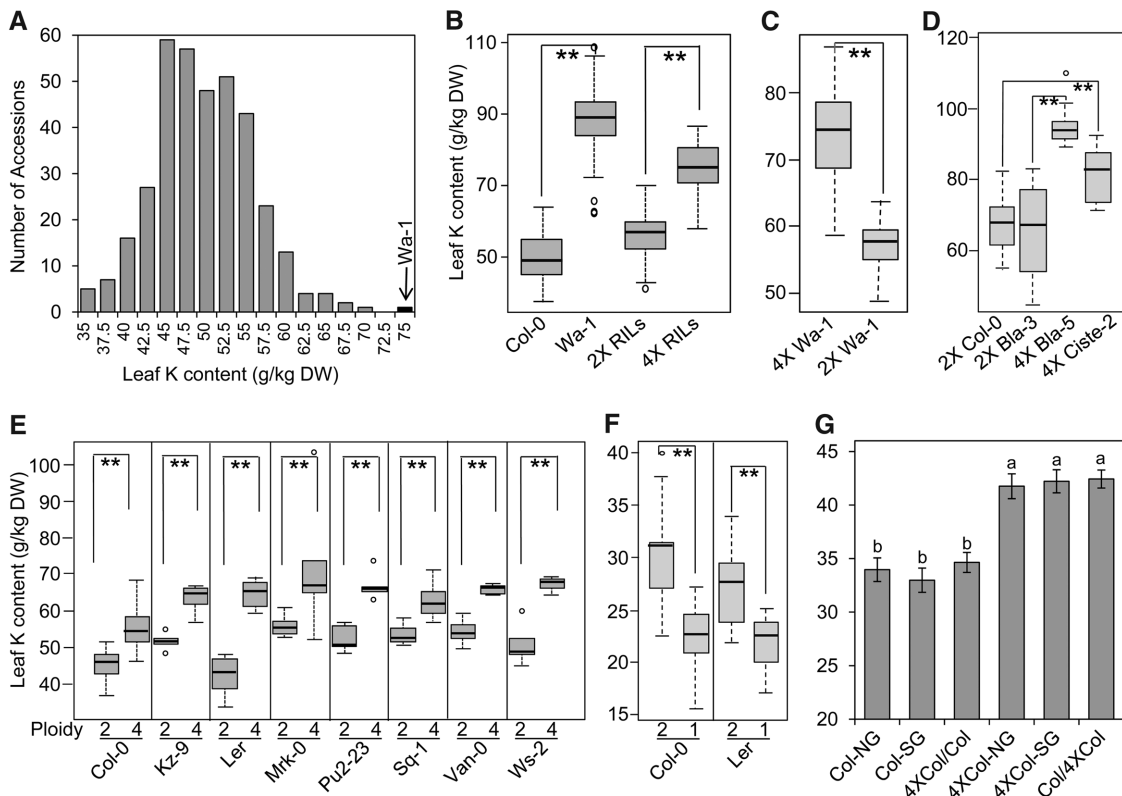Polyploidy, the quality of possessing multiple complete sets of chromosomes, is pervasive within land plants, suggesting an adaptive benefit though no mechanisms have been established (*1*). Soil discontinuities, such as boundaries between soil types, may underlie plant-selective constraints. In an analysis of the elemental composition of leaves from a set of 349 *Arabidopsis thaliana* accessions (*2*), the autotetraploid accession Wa-1 (from Warsaw, Poland) had the highest concentration of leaf potassium (K) (Fig. 1A) and the K analog rubidium (Rb) (fig. S1A). Recombinant inbred lines (RILs) between the diploid accession Col-0 and the autotetraploid Wa-1 (*3*) contain diploids and tetraploids with recombinant genotypes (*4*). All 89 RILs were phenotyped for the leaf concentration of K and Rb by inductively coupled plasma mass

[1]Institute of Biological and Environmental Sciences, University of Aberdeen, Cruickshank Building, St. Machar Drive, Aberdeen, AB24 3UU, UK. [2]Department of Horticulture and Landscape Architecture, Purdue University, West Lafayette, IN 47907, USA.

*Corresponding author. E-mail: david.salt@abdn.ac.uk

Fig. 1. Ploidy contributes to K accumulation in *A. thaliana* leaves. (**A**) Leaf K concentration among 349 accessions. The arrow and back bar indicate the tetraploid, Wa-1. DW, dry weight. (**B** to **F**) Box plots (the minimum, first quartile, median, third quartile, and maximum are shown, with data >1.5 interquartile ranges denoted with circles) for leaf K concentration in Col-0 x Wa-1 RILs (B), Wa-1 and diploid Wa-1 (C), natural tetraploid accessions (D), natural diploids and derived tetraploids (E), and natural diploids and derived haploids (F). (**G**) Leaf K concentration of grafted diploid and tetraploid plants. NG, nongrafted; SG, self-grafted; Col/4XCol, grafted with Col-0 as scion and 4XCol-0 as rootstock; 4XCol/Col, grafted with 4XCol-0 as scion and Col-0 as rootstock. Asterisks in (B) to (F) indicate the significance of pairwise comparisons (Student's *t* test; *$P <$ 0.05; **$P <$ 0.01). Letters above the bars in (G) indicate statistically different groups (one-way analysis of variance with groupings by Tukey's HSD with a 95% confidence interval). 2X, diploid; 4X, tetraploid. Data were collected from 6 to 18 biological replicates for each accession, cytotype or graft, and represented in (G) as mean ± SE. All leaf K concentration data are accessible using the digital object identifiers (DOIs) 10.4231/T9H41PBV and 10.4231/T93X84K7 (see http://dx.doi.org/).